Elastoplastic constitutive behavior and strain localization of a low-porosity sandstone during brittle fracturing

Shihuai Zhang[1]*, Pei Guo[2], Shunchuan Wu[2,3]

1. Department of Earth Sciences, ETH Zürich, 8092 Zürich, Switzerland

2. Key Laboratory of Ministry of Education for Efficient Mining and Safety of Metal Mines, University of Science and Technology Beijing, Beijing 100083, China.

3. Faculty of Land Resource Engineering, Kunming University of Science and Technology, Kunming, Yunnan 650093, China.

*Corresponding author: Shihuai Zhang (zhangshi@ethz.ch; shihuaizhang.xh1@gmail.com)

Keywords: Elastoplastic constitutive relations; Two-yield surface model; Strain localization; Low-porosity sandstone

Abstract

We investigated the elastoplastic behavior and strain localization of the Zigong sandstone (porosity: 6.5%) during brittle fracturing based on two series of axisymmetric compression experiments. The experiments were conducted under various confining pressures (σ_3 = 0 ~ 80 MPa). For each confining pressure, the sandstone specimens were deformed under constant axial and circumferential strain rates, respectively. When σ_3 < 60 MPa, the sandstone first undergoes stable deformation in the post-peak stage and then loses its stability. Before the emergence of instability, the mechanical behavior is hardly affected by the controlling method. When the confining is larger, the sandstone manifests a stable failure process during the whole loading stage. The observed elastoplastic behavior was described by a two-yield surface constitutive model established in the framework of generalized plastic mechanics. The proposed constitutive model incorporates two quadratic yield functions, as well as two linearly independent plastic potential functions, to honor the shear yield and volumetric dilatancy, respectively. Via the return mapping algorithm, the proposed constitutive model was verified by comparing the numerical results with experimental

results. In addition, the two-yield surface constitutive model, which is equivalent to the model proposed by Rudnicki and Rice,[1] was applied to localization analysis. Assuming that the onset of localization occurs at peak stress, frictional coefficient μ and dilatancy factor β were determined from experimental data. The variations of both plastic parameters predict the transition of localization mode from pure dilation bands under uniaxial compression to pure shear bands at high confining pressures, which is consistent with the experimental observations.

1. Introduction

The mechanical behavior of sandstone is intimately related to a variety of geologic processes and engineering applications. As with most of rocks, sandstone exhibits highly-nonlinear pressure dependence of its deformation, such as volumetric dilatancy and strain hardening/softening. Phenomenologically, the deformation process of sandstone subject to compression is typically accompanied by the development of planar deformation bands, also referred to as strain localization.[1] With the increase of pressure, strain localization varies the manifestations from dilation or shear bands in the brittle regime[2] to shear-enhanced compaction or homogenous cataclastic flow when entering the ductile regime.[3,4]

In order to understand these abundant mechanical properties, micromechanics and continuum mechanics are often utilized. The former generally includes acoustic emission[5–8] and thin section inspection.[9] It has been revealed that the progressive development of a macroscopic deformation band essentially depends on the initiation, growth, and coalescence of microcracks associated with the local stress heterogeneity. The increase of microcrack density can gradually degrade the rock sample, which ultimately shows a loss of strength and/or stability. The stability of the subsequent process (post-failure) depends mainly on the loading conditions and the stiffness of testing machine, which is essentially related to the elastic energy stored inside the rock.[10,11]

In the framework of plastic mechanics, it is required to establish a constitutive model that adequately incorporates the nonlinear characteristics of rocks, i.e., volumetric dilatancy and strain hardening/softening, so as to reproduce the deformation process of rocks. In particular, the phenomenon of strain localization can be regarded as a constitutive instability in an otherwise

homogenous material.[1] Therefore, the analysis of strain localization in rocks also entails an appropriate constitutive model. In their seminal work, Rudnicki and Rice[1] adopted a smooth yield function as defined by the Drucker-Prager criterion,[12] in which the material parameter μ (frictional coefficient) is a measure of the mean stress dependence of yielding. In addition to the equivalent plastic shear strain, used for keeping track of the history of plastic deformation, the introduction of a dilatancy factor (β) honors a non-associated flow rule and allows for volumetric dilatancy. Such a treatment is appropriate for accounting for the strain localization in low-porosity rocks. However, the selection of plastic potential function associated with shear yield is usually difficult and challenging.

In this study, we adopt the generalized plastic mechanics theory[13] to describe the mechanical behavior of a low-porosity sandstone, referred to as Zigong sandstone, under axisymmetric compression. In this theory, the single-yield surface model in the classical plastic mechanics is extended to a multiple-yield surface model, incorporating multiple plastic flow mechanisms. The plastic potential functions related to the yield surfaces can be selected arbitrarily as long as they are linearly independent. Specifically, we consider two fundamental plastic flow mechanisms, i.e., plastic shear and volumetric dilatancy, characteristic of brittle fracturing. The two-yield surface constitutive relationship is numerically integrated via return mapping algorithm, which shows good consistency with the experimental results. Moreover, we confirm that the proposed constitutive model is equivalent to the model proposed by Rudnicki and Rice[1] in the brittle regime. After investigating the effect of confining pressure on the strain localization mode, the proposed constitutive model is further validated by comparing with experimental observations.

2. Experiments and Results

2.1 Experimental Material and Experimental Procedure

Zigong sandstone represents a low-porosity (6.5%) hard sandstone composed mainly of silicate minerals, which has been systematically tested and investigated under different stress conditions.[8,14,15] Compared with other highly porous sandstones, Zigong sandstone features relatively higher strength and a wider brittle range.[15] It exhibits prominent characteristics of brittle fracturing even under a confining pressure (σ_3) of as high as 80 MPa, approximately corresponding

to a buried depth of 4 km.

The sandstone specimens were prepared as cylinders with 5 cm in diameter and 10 cm in height, following which they were dried at a temperature of 60 ℃ for 48 h. In this study, we present the results of two series of conventional triaxial compression (CTC) tests under various confining pressures (0 ~ 80 MPa, step: 10 MPa). In one series, termed as axial strain control (ASC) test, specimens were deformed under a constant axial strain rate (2.5×10^{-6} s^{-1}). In the other series, referred to as circumferential strain control (CSC) test, the axial force was applied by a constant rate (0.5 kN/s) up to 120 kN, which was then controlled by a constant circumferential strain (2×10^{-6} s^{-1}). For the two sets of uniaxial compression tests (σ_3 = 0 MPa), in particular, acoustic emission monitoring was elaborately implemented to capture the failure process.[8]

2.2 Stress-strain Curves and Characteristic Stress Thresholds

Figure 1 presents the stress-strain curves from the ASC and CSC tests, respectively. It can be seen that the mechanical behavior in the pre-peak stage is not significantly affected by the controlling methods (also see the comparison of stress thresholds in **Figure 2**). Over the peak strength, all specimens first display a negative post-peak modulus. According to Wawersik and Fairhurst,[10] such behavior (Class I) represents stable, controllable post-peak deformation. Since the amount of the elastic energy stored in the specimens is not sufficient to support the failure, it requires continuous loading for further deformation in this case. With the ongoing deformation, the failure process under low confining pressures tends to be unstable. Specifically, specimens in the ASC tests with σ_3 (= 0 ~ 60 MPa) show vertical stress drop (i.e., infinite post-peak modulus) as shown in **Figure 1a**. In the CSC tests, specimens under σ_3 (= 0 ~ 50 MPa) display a reduction in axial strain. The manifested positive post-peak modulus, defined as Class II behavior,[10] indicates an unstable and self-sustaining failure process. From the perspective of energy balance, the amount of the elastic energy stored in the specimens is much more than the requirement for failure, which would lead to an avalanche without withdrawing the exceeded energy. The discrete sampled data in both series show that both controlling methods cannot sustain the failure process in a stable manner, when σ_3 is less than 60 MPa. By contrast, when σ_3 is larger than 60 MPa, all specimens show stable failure process during the whole post-peak stage. In other words, Zigong sandstone features a combination of Class I and

Class II behavior under a low confining pressure and purely Class I behavior under a high confining pressure.

Based on these stress-strain curves, we can determine several characteristic stress thresholds, including crack initiation stress σ_{ci}, crack damage stress σ_{cd}, and peak stress σ_p, to characterize the deformation process.[16–18] Among them, the determination of σ_{ci} is essential to the construction of the constitutive model since it suggests the onset of plastic deformation. However, its determination has usually been subjective and of high uncertainty.[16,17,19–23] To circumvent this, we utilize an objective method called Lateral Strain Response (LSR) method[24] in this study. In addition, σ_{cd} and σ_p correspond to the point where volumetric strain curve reverses and the highest point of the stress-strain curve, respectively, which can be readily identified. **Figure 2** shows the determined values of σ_{ci}, σ_{cd} and σ_p and their positive dependence on σ_3. As alluded to above, the consistency between both series for each stress threshold indicates that the two control methods hardly affect the pre-peak behavior of Zigong sandstone. In addition, the peak strength of Zigong sandstone can be well captured by Hoek-Brown failure criterion and its extended 3D version.[15,25]

3. Elastoplastic Constitutive Properties of Zigong Sandstone

Instead of using a single-yield surface model, we adopt the generalized plastic theory[13] to establish a two-yield surface constitutive model for Zigong sandstone. In what follows, a brief introduction of the generalized plastic theory is first provided in Section 3.1. Based on the theoretical framework, we then explore the effect of confining pressure on the elastic shear and bulk moduli in Section 3.2. We propose a shear yield function and a volumetric yield function in Section 3.3 and Section 3.4, respectively, to include shear- and dilatancy-related plastic flow mechanisms. The two-yield constitutive model adopts non-associated flow rules and isotropic hardening rules.

3.1 Fundamentals of the Generalized Plastic Mechanics

Classic elastoplastic theory assumes that the total strain increment consists of elastic and plastic strain increments:

$$d\varepsilon_{ij} = d\varepsilon_{ij}^{e} + d\varepsilon_{ij}^{p} \tag{1}$$

in which the elastic strain increment $d\varepsilon_{ij}^{e}$ can be calculated by Hooke's law while the plastic strain

increment $d\varepsilon_{ij}^{p}$ is closely related to the plastic potential function Q by:

$$d\varepsilon_{ij}^{p} = d\lambda \frac{\partial Q}{\partial \sigma_{ij}} \tag{2}$$

in which $d\lambda$ is a non-negative scalar and σ_{ij} is the stress component. As pointed out by Zheng et al.[13], Eqn. 2 implies that the direction of the plastic strain increment depends only on stress states rather than stress increment, the latter of which has been experimentally observed in numerous geomaterials. In addition, the plastic potential function Q for geomaterials is usually difficult to determine according to the yield surface, i.e., following non-associated flow rule.

In the generalized plastic mechanics, three linearly-independent yield surfaces and corresponding plastic potential functions are assumed to be coexisting at any point in the stress space. In other words, the total plastic strain increment is the sum of the plastic strain increments of all of the yield surfaces. Consequently, the flow rule in the single-yield surface model can be generalized to:

$$d\varepsilon_{ij}^{p} = \sum_{k=1}^{3} d\lambda_{k} \frac{\partial Q_{k}}{\partial \sigma_{ij}} \tag{3}$$

in which the plastic potential functions Q_k can be any three linearly-independent functions, which jointly contribute to the total plastic strain increment. This advantage avails simple selection of the plastic potential functions and parameter fitting.

The magnitude of the plastic strain increment can be determined by the yield functions along with corresponding plastic strains. As alluded to in Section 2.2, the values of σ_{ci} of all tests depict the initial yield function $F(\sigma_{ij}) = 0$. Following this, the size, center, and shape of the yield surface will change with the ongoing loading, known as subsequent yield surface. To describe how an initial yield surface evolves to the subsequent yield surface, the hardening parameter H_α is imperative, which can be a function of plastic strains changing with deformation. Accordingly, assuming isotropic hardening, the subsequent yield surface can be expressed as:

$$F\left(\sigma_{ij}, H_{\alpha}\right) = 0 \tag{4}$$

Alternatively, if the von Mises equivalent stress q and mean stress p are used, the subsequent yield surface can be further given by:

$$F\left(p,q,\theta_\sigma,H_\alpha\right)=0 \tag{5}$$

where $p=\sigma_{ii}/3$, $q=\sqrt{3J_2}=\sqrt{3s_{ij}s_{ij}/2}$ with the stress deviator $s_{ij}=\sigma_{ij}-\sigma_{kk}\delta_{ij}/3$. δ_{ij} is the Kronecker symbol. θ_σ is the Lode angle, which is defined as $\theta_\sigma=\frac{1}{3}\sin^{-1}\left(-\frac{3\sqrt{3}}{2}\frac{J_3}{J_2^{3/2}}\right)$ with $J_3=\det\left(s_{ij}\right)$.

In the generalized plastic mechanics, therefore, the three yield surfaces can be presented by introducing different hardening parameters:

$$\begin{aligned} F_{\mathrm{v}}\left(p,q,\theta_\sigma,H_{\mathrm{v}}\right)&=0\\ F_q\left(p,q,\theta_\sigma,H_q\right)&=0\\ F_\theta\left(p,q,\theta_\sigma,H_\theta\right)&=0 \end{aligned} \tag{6}$$

which represent the volumetric yield function, shear yield function in q-direction, and shear yield function in θ_σ -direction, respectively. The hardening parameters can be further specified as functions of plastic volumetric strain $\varepsilon_{\mathrm{v}}^p$, plastic shear strain in q-direction (γ_q^p) and in θ_σ -direction (γ_θ^p), respectively.

Considering the consistency condition, the stress state should be always located on the yield surfaces to ensure continuous plastic deformation. By differentiating Eqn. 6, we have:

$$\begin{bmatrix} d\varepsilon_{\mathrm{v}}^p\\ d\gamma_q^p\\ d\gamma_\theta^p \end{bmatrix}=\begin{bmatrix} \frac{1}{A_{\mathrm{v}}}\frac{\partial F_{\mathrm{v}}}{\partial p} & \frac{1}{A_{\mathrm{v}}}\frac{\partial F_{\mathrm{v}}}{\partial q} & \frac{1}{A_{\mathrm{v}}}\frac{\partial F_{\mathrm{v}}}{\partial \theta_\sigma}\\ \frac{1}{A_q}\frac{\partial F_q}{\partial p} & \frac{1}{A_q}\frac{\partial F_q}{\partial q} & \frac{1}{A_q}\frac{\partial F_q}{\partial \theta_\sigma}\\ \frac{1}{A_\theta}\frac{\partial F_\theta}{\partial p} & \frac{1}{A_\theta}\frac{\partial F_\theta}{\partial q} & \frac{1}{A_\theta}\frac{\partial F_\theta}{\partial \theta_\sigma} \end{bmatrix}\begin{bmatrix} dp\\ dq\\ d\theta_\sigma \end{bmatrix} \tag{7}$$

in which $A_{\mathrm{v}}=-\frac{\partial F_{\mathrm{v}}}{\partial H_{\mathrm{v}}}\frac{\partial H_{\mathrm{v}}}{\partial \varepsilon_{\mathrm{v}}^p}$, $A_q=-\frac{\partial F_q}{\partial H_q}\frac{\partial H_q}{\partial \gamma_q^p}$, $A_\theta=-\frac{\partial F_\theta}{\partial H_\theta}\frac{\partial H_\theta}{\partial \gamma_\theta^p}$. Since the effect of Lode angle θ_σ is always little on the mechanical behavior of geomaterials, Eqn. 7 can be reduced to:

$$\begin{bmatrix} d\varepsilon_{\mathrm{v}}^p\\ d\gamma_q^p \end{bmatrix}=\begin{bmatrix} \frac{1}{A_{\mathrm{v}}}\frac{\partial F_{\mathrm{v}}}{\partial p} & \frac{1}{A_{\mathrm{v}}}\frac{\partial F_{\mathrm{v}}}{\partial q}\\ \frac{1}{A_q}\frac{\partial F_q}{\partial p} & \frac{1}{A_q}\frac{\partial F_q}{\partial q} \end{bmatrix}\begin{bmatrix} dp\\ dq \end{bmatrix} \tag{8}$$

3.2 Effect of Confining Pressure on the Elastic Properties

According to the notations in Eqn. 5 to Eqn. 8, we specially transform the principal stresses to von Mises equivalent stress q and mean stress p. For strains, we use the generalized shear strain γ and volumetric strain ε_v, which are defined as:

$$\gamma = \frac{\sqrt{2}}{3}\sqrt{(\varepsilon_1 - \varepsilon_2)^2 + (\varepsilon_2 - \varepsilon_3)^2 + (\varepsilon_1 - \varepsilon_3)^2} \tag{9}$$

$$\varepsilon_v = \varepsilon_1 + \varepsilon_2 + \varepsilon_3 \tag{10}$$

where ε_1, ε_2, ε_3 are the three principal strains.

Consequently, the stress-strain curves in **Figure 1** can be plotted as q-γ and p-ε_v curves, which enable the determination of elastic shear (G) and bulk (K) moduli, respectively, based on the determined values of σ_{ci}. In **Figure 3**, the effect of confining pressure on G and K is shown. It is found that, for both elastic moduli, the results of the CSC tests are consistently larger than that obtained from the ASC tests. The mean values of both G and K show an increase-then-decrease trend, which can be fit by the following parabolic functions (black curves in **Figure 3**):

$$G = a_G(\sigma_3)^2 + b_G\sigma_3 + c_G \tag{11}$$

$$K = a_K(\sigma_3)^2 + b_K\sigma_3 + c_K \tag{12}$$

in which the material parameters are given as: a_G = -9.568×10^{-4}, b_G = 0.1165, c_G = 8.956; a_K = -2.135×10^{-3}, b_K = 0.2178, c_K = 12.02.

With the determined elastic moduli, we are further able to calculate the plastic shear (γ_q^p) and volumetric (ε_v^p) strains, which are plotted in **Figure 4** in relation to q. In the following two sections, a shear yield function and volumetric yield function will be proposed based on the curves in **Figure 4**.

3.3 Shear yield surface and hardening function

The plastic shear strain γ_q^p is selected as an internal variable for the shear yield mechanism. Specifically, a series of plastic shear strain values are selected, which give the contours of the plastic shear strain in the p-q plane. Note that, the data corresponding to the unstable failure process is not included since the testing system failed to record reliably. As shown in **Figure 5a**, these contours are essentially the shear yield surfaces. As the plastic shear strain increases, the shear yield surface

first increases then decreases (i.e., strain softening, which is not explicitly exemplified in **Figure 5a**). To quantitatively describe these shear yield surfaces, an expression similar to the form of Hoek-Brown failure criterion is employed:

$$F_q\left(p, q, H_q\right) = 3q^2 + m_s H_q q - 3H_q^2 - 3m_s H_q p = 0 \tag{13}$$

where m_s is the material parameter. By fitting to the test data, it is found that m_s can be approximately selected as 10 for Zigong sandstone.

For each confining pressure, the average values of the ASC and CSC tests are utilized to obtain the relationship between H_q and γ_q^p. As shown in **Figure 5b**, such relationship features a transition from strain hardening to softening as γ_q^p increases for all confining pressures. Accordingly, the following function is proposed for hardening rule:

$$H_q = a_q \log\left(b_q \gamma_q^p + 1\right) + c_q \gamma_q^p + d_q \tag{14}$$

where a_q, b_q, c_q, and d_q are constants. Based on the curves in **Figure 5b**, each of these constants is given as a function of σ_3:

$$\begin{aligned} a_q &= -0.02571\left(\sigma_3\right)^2 + 2.577\sigma_3 + 35.98 \\ b_q &= \left(1.542\times10^5\right)\exp\left(-0.296\sigma_3\right) + 9453\exp\left(-0.01237\sigma_3\right) \\ c_q &= -0.68\left(\sigma_3\right)^2 - 31.67\sigma_3 - \left(7.303\times10^3\right) \\ d_q &= 0.215\sigma_3 + 40 \end{aligned} \tag{15}$$

As suggested by the generalized plastic mechanics theory, a simple plastic potential function for shear deformation can be selected applying the non-associated flow rule:

$$Q_q = q \tag{16}$$

3.4 Dilatant Volumetric yield surface and hardening function

In the previous section, the hardening effect is ascribed to the plastic shear strain. Since deformation in low-porosity rocks during brittle fracturing is also characterized by volumetric dilatancy,[19] a series of volumetric yield surfaces incorporating dilatant plastic volumetric change is proposed. As implied by **Figure 4**, Zigong sandstone does not show any volumetric compaction when confining pressure increases up to 80 MPa. Therefore, the volumetric compaction mechanism, specific to the 'cap' model for porous rocks[3,26] is not considered in this study.

To describe the volumetric yield surface, the plastic volumetric strain $\varepsilon_{\mathrm{V}}^{p}$ is utilized as the internal variable. In **Figure 6a**, the obtained volumetric yield surfaces are similar to the shear yield surfaces in **Figure 5a**. Hence, Eqn. 13 can also be used but with different hardening parameter H_{v}:

$$F_{\mathrm{v}}\left(p,q,H_{\mathrm{v}}\right)=3q^{2}+m_{s}H_{\mathrm{v}}q-3H_{\mathrm{v}}^{2}-3m_{s}H_{\mathrm{v}}p=0 \tag{17}$$

in which the approximation of m_s = 10 is also found to be appropriate. The relationship between the hardening parameter H_{v} and plastic volumetric strain $\varepsilon_{\mathrm{v}}^{p}$ is fit using the expression of Eqn. 14 with a new set of parameters:

$$\begin{aligned}
a_{\mathrm{v}} &= -0.01371\left(\sigma_{3}\right)^{2}+1.133\sigma_{3}+51.87\\
b_{\mathrm{v}} &= -9.426\left(\sigma_{3}\right)^{2}+537.3\sigma_{3}-(1.829\times10^{4})\\
c_{\mathrm{v}} &= 0.2956\left(\sigma_{3}\right)^{2}+1.739\sigma_{3}+(5.716\times10^{3})\\
d_{\mathrm{v}} &= 0.1233\sigma_{3}+38.82
\end{aligned} \tag{18}$$

Employing a non-associated flow rule, the plastic potential function can be simply proposed as:

$$Q_{\mathrm{v}}=p \tag{19}$$

Note that the two plastic potential functions, i.e., Eqn. 16 and Eqn. 19, are linearly independent as mandated by the theory of generalized plasticity mechanics.

4 Summary and Validation of the Elastoplastic Constitutive Relationship

4.1 General Form of the Elastoplastic Constitutive Relationship

Based on the above derivations, the elastoplastic constitutive relationship of Zigong sandstone can be derived with the assumption of small strain. Firstly, with the proposed two plastic potential functions, the flow rule in Eqn. 3 is now expressed as:

$$d\boldsymbol{\varepsilon}^{p}=d\lambda_{1}\frac{\partial Q_{\mathrm{v}}}{\partial\boldsymbol{\sigma}}+d\lambda_{2}\frac{\partial Q_{q}}{\partial\boldsymbol{\sigma}} \tag{20}$$

in which stress and strain are expressed in matrix form with $\boldsymbol{\varepsilon}^{p}=\left[\varepsilon_{\mathrm{v}}^{p},\gamma_{q}^{p}\right]^{T}$ and $\boldsymbol{\sigma}=\left[p,q\right]^{T}$. In addition, it can be proved that $d\varepsilon_{\mathrm{v}}^{p}=d\lambda_{1}$ and $d\gamma_{q}^{p}=d\lambda_{2}$.

Recalling the additivity of elastic and plastic strains, Eqn. 1 can be alternatively expressed as:

$$d\boldsymbol{\varepsilon}=d\boldsymbol{\varepsilon}^{e}+d\boldsymbol{\varepsilon}^{p}=d\boldsymbol{\varepsilon}^{e}+d\varepsilon_{\mathrm{v}}^{p}\frac{\partial Q_{\mathrm{v}}}{\partial\boldsymbol{\sigma}}+d\gamma_{q}^{p}\frac{\partial Q_{q}}{\partial\boldsymbol{\sigma}} \tag{21}$$

Consequently, the elastic response is defined by:

$$d\boldsymbol{\sigma} = \mathbf{D}^e \left(d\boldsymbol{\varepsilon} - d\varepsilon_{\mathrm{v}}^p \frac{\partial Q_{\mathrm{v}}}{\partial \boldsymbol{\sigma}} - d\gamma_q^p \frac{\partial Q_q}{\partial \boldsymbol{\sigma}} \right) \tag{22}$$

where $\mathbf{D}^e = \begin{bmatrix} K & \\ & 3G \end{bmatrix}$ is the elastic stiffness matrix.

The consistency condition (or Eqn. 8) implies the following loading/unloading conditions:

$$\begin{cases} F_{\mathrm{v}} \le 0, \quad d\varepsilon_{\mathrm{v}}^p \ge 0, \quad d\varepsilon_{\mathrm{v}}^p F_{\mathrm{v}} = 0 \\ F_q \le 0, \quad d\gamma_q^p \ge 0, \quad d\gamma_q^p F_q = 0 \end{cases} \tag{23}$$

which are often called Kuhn-Tucker complementary conditions. For each yield surface, the first term indicates that the stress state must lie on or within the yield surface while the second term suggests that the plastic strain increment is always non-negative. The last term assures that the stress state remains on the current yield surface during plastic loading. Then the consistency condition can be stated as:

$$\begin{cases} d\varepsilon_{\mathrm{v}}^p \cdot dF_{\mathrm{v}} = 0, \text{ if } F_{\mathrm{v}} = 0 \\ d\gamma_q^p \cdot dF_q = 0, \text{ if } F_q = 0 \end{cases} \tag{24}$$

Hence, if $d\gamma_q^p$ and $d\varepsilon_{\mathrm{v}}^p$ are both positive, it follows that $dF_q = dF_{\mathrm{v}} = 0$. As a result, substitution of the matrix form of Eqn. 8 into Eqn. 22 yields:

$$\begin{cases} \left(1 + \frac{1}{A_{\mathrm{v}}} \left(\frac{\partial F_{\mathrm{v}}}{\partial \boldsymbol{\sigma}} \right)^T \mathbf{D}^e \frac{\partial Q_{\mathrm{v}}}{\partial \boldsymbol{\sigma}} \right) d\varepsilon_{\mathrm{v}}^p = \frac{1}{A_{\mathrm{v}}} \left(\frac{\partial F_{\mathrm{v}}}{\partial \boldsymbol{\sigma}} \right)^T \mathbf{D}^e \left(d\boldsymbol{\varepsilon} - d\gamma_q^p \frac{\partial Q_q}{\partial \boldsymbol{\sigma}} \right) \\ \left(1 + \frac{1}{A_q} \left(\frac{\partial F_q}{\partial \boldsymbol{\sigma}} \right)^T \mathbf{D}^e \frac{\partial Q_q}{\partial \boldsymbol{\sigma}} \right) d\gamma_q^p = \frac{1}{A_q} \left(\frac{\partial F_q}{\partial \boldsymbol{\sigma}} \right)^T \mathbf{D}^e \left(d\boldsymbol{\varepsilon} - d\varepsilon_{\mathrm{v}}^p \frac{\partial Q_{\mathrm{v}}}{\partial \boldsymbol{\sigma}} \right) \end{cases} \tag{25}$$

Solving for $d\gamma_q^p$ and $d\varepsilon_{\mathrm{v}}^p$, we have:

$$d\varepsilon_{\mathrm{v}}^p = \frac{\eta_1 A_q + \eta_1 \eta_4 - \eta_2 \eta_5}{A_q A_{\mathrm{v}} + \eta_3 A_q + \eta_4 A_{\mathrm{v}} + \eta_3 \eta_4 - \eta_2 \eta_6} \tag{26}$$

$$d\gamma_q^p = \frac{\eta_5 A_{\mathrm{v}} + \eta_3 \eta_5 - \eta_1 \eta_6}{A_q A_{\mathrm{v}} + \eta_3 A_q + \eta_4 A_{\mathrm{v}} + \eta_3 \eta_4 - \eta_2 \eta_6} \tag{27}$$

with the following definitions:

$$\eta_1=\left(\frac{\partial F_{\mathrm{v}}}{\partial \boldsymbol{\sigma}}\right)^T \mathbf{D}^e d\boldsymbol{\varepsilon},\quad \eta_2=\left(\frac{\partial F_{\mathrm{v}}}{\partial \boldsymbol{\sigma}}\right)^T \mathbf{D}^e \frac{\partial Q_q}{\partial \boldsymbol{\sigma}},\quad \eta_3=\left(\frac{\partial F_{\mathrm{v}}}{\partial \boldsymbol{\sigma}}\right)^T \mathbf{D}^e \frac{\partial Q_{\mathrm{v}}}{\partial \boldsymbol{\sigma}}$$
$$\eta_4=\left(\frac{\partial F_q}{\partial \boldsymbol{\sigma}}\right)^T \mathbf{D}^e \frac{\partial Q_q}{\partial \boldsymbol{\sigma}},\quad \eta_5=\left(\frac{\partial F_q}{\partial \boldsymbol{\sigma}}\right)^T \mathbf{D}^e d\boldsymbol{\varepsilon},\quad \eta_6=\left(\frac{\partial F_q}{\partial \boldsymbol{\sigma}}\right)^T \mathbf{D}^e \frac{\partial Q_{\mathrm{v}}}{\partial \boldsymbol{\sigma}} \tag{28}$$

Then substituting Eqns. 26 and 27 into Eqn. 22, the general elastoplastic constitutive relationship takes the form:

$$d\boldsymbol{\sigma} = \mathbf{D}^{ep} d\boldsymbol{\varepsilon} \tag{29}$$

where $\mathbf{D}^{ep}$ is the elastoplastic stiffness matrix:

$$\mathbf{D}^{ep}=\mathbf{D}^e-\frac{\mathbf{D}^e\left[\frac{\partial Q_{\mathrm{v}}}{\partial \boldsymbol{\sigma}}\left(\left(A_q+\eta_4\right)\left(\frac{\partial F_{\mathrm{v}}}{\partial \boldsymbol{\sigma}}\right)^T-\eta_2\left(\frac{\partial F_q}{\partial \boldsymbol{\sigma}}\right)^T\right)+\frac{\partial Q_q}{\partial \boldsymbol{\sigma}}\left(\left(A_{\mathrm{v}}+\eta_3\right)\left(\frac{\partial F_q}{\partial \boldsymbol{\sigma}}\right)^T-\eta_6\left(\frac{\partial F_{\mathrm{v}}}{\partial \boldsymbol{\sigma}}\right)^T\right)\right]\mathbf{D}^e}{A_q A_{\mathrm{v}}+\eta_3 A_q+\eta_4 A_{\mathrm{v}}+\eta_3\eta_4-\eta_2\eta_6} \tag{30}$$

When the model is in the elastic regime, $\mathbf{D}^{ep}$ is simply equal to $\mathbf{D}^e$.

The above expressions complete the general mathematical formulation of the proposed two-yield surface constitutive model for Zigong sandstone. Note that, Eqn. 30 can be flexibly reduced to the single surface formulation via leaving out the terms associated with the inactivated yield surface.

4.2 Numerical Integration of the Proposed Elastoplastic Constitutive Relations

In this section, the proposed constitutive relations are validated by comparing with the experimental data. Unlike the linear elasticity, the elastoplastic constitutive relations are nonlinear and not analytically integrable. Therefore, numerical integration is required to define the resulting mechanical response. Among many techniques for numerical integration,[27] the return mapping algorithm is particularly adopted in this study.

Implementation of the return mapping algorithm is essential to find the numerical solution of a nonlinear problem about stress/strain update. Specifically, for a prescribed loading path, we need to find the respective increments of stress $\boldsymbol{\sigma}$, strain $\boldsymbol{\varepsilon}$, and hardening parameter H_α (the subscript α = v or q) at each loading step according to the elastoplastic constitutive relations. The problem can be further formulated in discrete forms by using the backward Euler method as:

$$\begin{cases} \boldsymbol{\varepsilon}_{n+1} = \boldsymbol{\varepsilon}_n + \Delta\boldsymbol{\varepsilon} \\ \boldsymbol{\varepsilon}^p_{n+1} = \boldsymbol{\varepsilon}^p_n + \Delta\boldsymbol{\varepsilon}^p_{n+1} \\ \boldsymbol{\sigma}_{n+1} = \mathbf{D}^e\left(\boldsymbol{\varepsilon}_{n+1} - \boldsymbol{\varepsilon}^p_{n+1}\right) \\ H_{\alpha,n+1} = H_\alpha\left(\boldsymbol{\varepsilon}^p_{n+1}\right) \end{cases} \tag{31}$$

in which the three variables $\{\boldsymbol{\sigma}, \boldsymbol{\varepsilon}^p, H_\alpha\}_n$ are known at the current step n and $\Delta\boldsymbol{\varepsilon}^p_{n+1}$ is the unknown to be determined. In addition, the Kuhn-Tucker conditions are given by:

$$F_\alpha\left(\boldsymbol{\sigma}_{n+1}, H_{\alpha,n+1}\right) \le 0, \quad \Delta\boldsymbol{\varepsilon}^p_{n+1} \ge 0, \quad \Delta\boldsymbol{\varepsilon}^p_{n+1} F_\alpha\left(\boldsymbol{\sigma}_{n+1}, H_{\alpha,n+1}\right) = 0 \tag{32}$$

To address this nonlinear optimization problem, the return mapping algorithm generally involves two steps: (1) trial elastic prediction; and (2) plastic correction returning the trial state to the current yield surface. During the integration process, the strain increment $\Delta\boldsymbol{\varepsilon}$ is fixed for each loading step. The trial elastic prediction can be obtained by taking:

$$\begin{cases} \boldsymbol{\varepsilon}_{n+1} = \boldsymbol{\varepsilon}_n + \Delta\boldsymbol{\varepsilon} \\ \boldsymbol{\varepsilon}^p_{n+1} = \boldsymbol{\varepsilon}^p_n \\ H^{trial}_{\alpha,n+1} = H_{\alpha,n} \end{cases} \tag{33}$$

and the trial stress state is given by:

$$\boldsymbol{\sigma}^{trial}_{n+1} = \boldsymbol{\sigma}_n + \mathbf{D}^e \Delta\boldsymbol{\varepsilon} \tag{34}$$

This process is illustrated in **Figure 7a** as Path I. Then the Kuhn-Tucker conditions are checked: If $F_\alpha\left(\boldsymbol{\sigma}^{trial}_{n+1}, H^{trial}_{\alpha,n+1}\right) \le 0$, the trial stress state is purely elastic and $\Delta\boldsymbol{\varepsilon}^p_{n+1} = 0$; if $F_\alpha\left(\boldsymbol{\sigma}^{trial}_{n+1}, H^{trial}_{\alpha,n+1}\right) > 0$, the trial stress state is outside the current yield surface (**Figure 7a**) and $\Delta\boldsymbol{\varepsilon}^p_{n+1}$ must be solved to facilitate returning stresses to the yield surface.

As indicated by Eqns. 31 and 32, the value of $\Delta\boldsymbol{\varepsilon}^p_{n+1}$ cannot be solved explicitly since they collectively represent a complex nonlinear optimization problem. Therefore, the Newton-Raphson method is utilized here to iteratively find the numerical solution:

$$\begin{cases} F^k_\alpha + \left(\dfrac{\partial F_\alpha}{\partial \Delta\boldsymbol{\varepsilon}^p_{n+1}}\right)^k \delta\left(\Delta\boldsymbol{\varepsilon}^p_{n+1}\right)^k = 0 \\ \left(\Delta\boldsymbol{\varepsilon}^p_{n+1}\right)^{k+1} = \left(\Delta\boldsymbol{\varepsilon}^p_{n+1}\right)^k + \delta\left(\Delta\boldsymbol{\varepsilon}^p_{n+1}\right)^k \end{cases} \tag{35}$$

where $\delta\left(\Delta\boldsymbol{\varepsilon}^p_{n+1}\right)^k$ is the increment of $\Delta\boldsymbol{\varepsilon}^p_{n+1}$ at the kth iteration. This iterative process (Path II) is also geometrically illustrated in **Figure 7a**. With the determined $\Delta\boldsymbol{\varepsilon}^p_{n+1}$, the loading step is simply

represented by Path III. Furthermore, the application of the return mapping algorithm to the shear yield function is shown in **Figure 7b** as an example.

Applying the return mapping algorithm to the proposed elastoplastic constitutive relationship, we are able to perform the numerical simulations. As shown in **Figure 8**, the numerical results show a good agreement with the experimental results under different confining pressures. The proposed elastoplastic constitutive model is able to capture the mechanical properties (i.e., strain hardening, strain softening, dilatancy, and confining pressure effect) of Zigong sandstone. However, since the unstable post-peak stage and frictional sliding are not included in the constitutive model, the complete stress-strain curves are not shown.

5. Analysis of Strain Localization in Zigong Sandstone

In this section, strain localization and its pressure dependence are investigated in the framework of the proposed constitutive model for Zigong sandstone. The proposed two-yield surface model explicitly considers shear yield and volumetric dilatancy during brittle fracturing, which facilitates the description of stress-strain relations. By contrast, Rudnicki and Rice[1] (hereafter referred to as RR model) considers only shear yield in the bifurcation theory while the volumetric dilatancy is included by introducing the dilatancy factor (β). In the following, we first demonstrate the proposed two-yield surface model is equivalent to the RR model in the brittle regime. Then we examine the observed strain localization in Zigong sandstone under different confining pressures.

5.1 Equivalence of the Proposed Constitutive Model to RR Model

In order to compare with the classical RR model, we rewrite Eqn. 20 as:

$$\begin{aligned} d\varepsilon_{ij}^{p} &= d\varepsilon_{\mathrm{v}}^{p}\frac{\partial Q_{\mathrm{v}}}{\partial p}\frac{\partial p}{\partial \sigma_{ij}} + d\gamma_{q}^{p}\frac{\partial Q_{q}}{\partial q}\frac{\partial q}{\partial \sigma_{ij}} \\ &= d\varepsilon_{\mathrm{v}}^{p}\frac{\partial p}{\partial \sigma_{ij}} + d\gamma_{q}^{p}\frac{\partial q}{\partial \sigma_{ij}} \end{aligned} \tag{36}$$

Substitution of $\left(\partial p/\partial \sigma_{ij}\right)=\frac{1}{3}\delta_{ij}$ and $\left(\partial q/\partial \sigma_{ij}\right)=\frac{s_{ij}}{2q}$ into Eqn. 36 gives:

$$d\varepsilon_{ij}^{p} = d\varepsilon_{\mathrm{v}}^{p}\left(\frac{1}{3}\delta_{ij}\right) + d\gamma_{q}^{p}\left(\frac{s_{ij}}{2q}\right) \tag{37}$$

Invoking the definition of the dilatancy factor $\beta = -d\varepsilon_{\mathrm{v}}^{p}/d\gamma_{q}^{p}$, we have:

$$d\varepsilon_{ij}^{p} = d\gamma_{q}^{p}\left(\frac{s_{ij}}{2q} - \frac{1}{3}\beta\delta_{ij}\right) \tag{38}$$

in which $d\gamma_q^p$ has been defined in Eqn. 8. Consequently, Eqn. 38 can be further expressed as:

$$d\varepsilon_{ij}^{p} = \frac{1}{H}\left(\frac{s_{ij}}{2q} - \frac{1}{3}\beta\delta_{ij}\right)\left(\frac{s_{kl}}{2q} - \frac{1}{3}\mu\delta_{kl}\right)d\sigma_{kl} \tag{39}$$

in which the term $H = A_q \big/ \left(\partial F_q / \partial q\right)$ is the plastic hardening modulus as commonly used in the RR model.[26,28] The frictional coefficient μ is defined as the local slope of the shear yield surface $\mu = -\dfrac{\partial F_q}{\partial p} \Big/ \dfrac{\partial F_q}{\partial q}$. Obviously, the proposed constitutive model is equivalent to the RR model. It is also noteworthy that volumetric compressive mechanism can also be incorporated to model the yield 'cap', which, however, needs more complicated algebraic manipulation to apply the bifurcation theory [29].

5.2 Effect of Confining Pressure on Strain Localization Mode

As indicated by the RR model, the three plastic parameters (μ, β, H) are relevant when applying the bifurcation theory to strain localization. Since the plastic hardening modulus H is a function of the orientation of the potential band and decreases monotonically with the ongoing plastic deformation, Rudnicki and Rice[1] proposed the definition of critical hardening modulus h_{cr}:

$$\frac{h_{cr}}{G} = \frac{1+\nu}{9(1-\nu)}(\beta-\mu)^2 - \frac{1+\nu}{2}\left[N + \frac{1}{3}(\beta+\mu)\right]^2 \tag{40}$$

in which N represents the state of deviatoric stress, ranging from $-1/\sqrt{3}$ for axisymmetric extension, through 0 for pure shear to $1/\sqrt{3}$ for axisymmetric compression. When H decreases to the value of h_{cr}, strain localization occurs.

Alternatively, the following condition is given for the onset of shear band[30,31]:

$$(1-2\nu)N - \sqrt{4-3N^2} \le \frac{2}{3}(1+\nu)(\beta+\mu) \le (1-2\nu)N + \sqrt{4-3N^2} \tag{41}$$

When the left inequality is violated, compaction band would emerge; while dilation band would occur when the right inequality is not satisfied.

With these conditions, we are able to investigate the effect of confining pressure on the strain localization mode of Zigong sandstone by evaluating parameters μ and β. In **Figure 9**, the plastic volumetric strain ε_v^p vs. plastic shear strain γ_q^p curves are presented for both ASC and CSC tests. All curves show that the relation between ε_v^p and γ_q^p is quasi-linear, enabling the fit of β in a simple manner. Apparently, β decreases with the increase of confining pressure, suggesting that the sandstone undergoes more compactive deformation, as also implied by **Figure 8**.

In **Figure 10**, we further show the variations of the frictional coefficient μ with the plastic shear strain γ_q^p and confining pressure. For each axisymmetric compression test, μ rapidly increases with γ_q^p then reaches a plateau near the peak strength. On the other hand, μ shows a decreasing trend as confining pressure increases. As implied by the acoustic emission characteristics revealed in uniaxial compression tests[8], strain localization is most likely to develop in the post-peak stage for Zigong sandstone during brittle fracturing. Therefore, values of frictional coefficient μ and corresponding to the peak strength are used to characterize the onset of strain localization.

Figure 11 summarizes the values of β and μ under different confining pressures. As indicated by **Figure 9** and **Figure 10**, both constitutive parameters decrease with increasing confining pressure, and β is typically less than μ. The inequality of both constitutive parameters suggests that the flow rule for Zigong sandstone should be non-associated. In addition, the localization analysis predicts that the decreasing constitutive parameters are accompanied by the transition of the localization mode. Localization with the values of β and μ dissatisfying the right inequality of Eqn. 41 would be in the form of dilation bands. In **Figure 11**, this condition is indicated by using three values of Poisson's ratio (ν = 0.1, 0.2, and 0.3) as a reference, since the value of Poisson's ratio is closely dependent on confining pressure. It can be seen that the theoretical prediction supports pure dilation bands for the sandstone under uniaxial compression, which is consistent with the experimental observations.[8] Given that the values of Poisson's ratio of Zigong sandstone range from 0.2 to 0.3, it is predicted that the sandstone still has the potential to develop dilation bands when σ_3 = 10 and 20 MPa. When confining pressure further increases, pure shear bands are predicted, in good accordance with experimental observations.[15] Finally, the sandstone is far from ductile regime under the

experimental conditions. Compared with other porous sandstones, Zigong sandstone features a wide brittle range due to its low porosity.[15]

6. Conclusions

We conducted two series of axisymmetric compression experiments in the low-porosity Zigong sandstone under various confining pressures (0 ~ 80 MPa with a step of 10 MPa). For each confining pressure, sandstone specimens were deformed under constant axial and circumferential strain rates, respectively. It is found that the Zigong sandstone features a combination of Class I (stable) and Class II (unstable) behavior in the post-peak stage under a low confining pressure (< 60 MPa) and purely Class I behavior for a high confining pressure.

Based on the theory of generalized plastic mechanics, a two-yield surface elastoplastic constitutive model was proposed to describe the deformation characteristics of the sandstone. The proposed elastoplastic constitutive model employs two quadratic yield functions, along with two linearly independent plastic potential functions, to honor shear yield and volumetric dilatancy, respectively. Numerical integration of the constitutive relations was carried out using the return mapping algorithm. It is found that the resulting stress-strain relations are in good agreement with the experimental results. It can be concluded that the proposed model adequately captures the elastoplastic behavior (i.e., strain hardening, strain softening, dilatancy, and confining pressure effect) of Zigong sandstone in the brittle regime.

In the context of brittle fracturing, it is demonstrated that the proposed two-yield surface model is essentially equivalent to the single-yield surface model proposed by Rudnicki and Rice[1] for strain localization analysis. In addition, formulations of three relevant plastic parameters (μ, β, H) were derived according to the proposed constitutive equations. To analyze strain localization, the effects of plastic deformation and confining pressure on parameters μ and β were investigated. As plastic deformation accumulates, β is relatively constant, while μ increases rapidly and reaches a plateau subsequently. With increasing confining pressure, both μ and β decrease, and μ is always larger than β. The theoretical predictions indicate that the localization mode in Zigong sandstone undergoes a transition from pure dilation bands under uniaxial compression to pure shear bands at high confining pressures.

Acknowledgments

We are grateful to the Editor and anonymous reviewers for their insightful comments and constructive suggestions to improve this manuscript. The support provided by the China Scholarship Council (No. 202006460039) is greatly appreciated by Pei Guo. Shunchuan Wu acknowledges the National Natural Science Foundation of China (No.51934003), Program for Innovative Research Team (in Science and Technology) in University of Yunnan Province, and Yunnan innovation team (202105AE160023)

References

1. Rudnicki JW, Rice JR. Conditions for the localization of deformation in pressure-sensitive dilatant materials. *J Mech Phys Solids*. 1975;23(6):371-394. doi:10.1016/0022-5096(75)90001-0

2. Bésuelle P, Desrues J, Raynaud S. Experimental characterisation of the localisation phenomenon inside a Vosges sandstone in a triaxial cell. *Int J Rock Mech Min Sci*. 2000;37(8):1223-1237. doi:10.1016/S1365-1609(00)00057-5

3. Baud P, Vajdova V, Wong T. Shear-enhanced compaction and strain localization: Inelastic deformation and constitutive modeling of four porous sandstones. *J Geophys Res Solid Earth*. 2006;111(B12):B12401. doi:10.1029/2005JB004101

4. Wong T, David C, Zhu W. The transition from brittle faulting to cataclastic flow in porous sandstones: Mechanical deformation. *J Geophys Res Solid Earth*. 1997;102(B2):3009-3025. doi:10.1029/96jb03281

5. Zang A, Wagner CF, Dresen G. Acoustic emission, microstructure, and damage model of dry and wet sandstone stressed to failure. *J Geophys Res B Solid Earth*. 1996;101(8):17507-17521. doi:10.1029/96jb01189

6. Fortin J, Stanchits S, Dresen G, Guéguen Y. Acoustic emission and velocities associated with the formation of compaction bands in sandstone. *J Geophys Res*. 2006;111(B10):B10203. doi:10.1029/2005JB003854

7. Ingraham MD, Issen KA, Holcomb DJ. Response of Castlegate sandstone to true triaxial states of stress. *J Geophys Res Solid Earth*. 2013;118(2):536-552. doi:10.1002/jgrb.50084

8. Zhang S, Wu S, Chu C, Guo P, Zhang G. Acoustic Emission Associated with Self-Sustaining Failure in Low-Porosity Sandstone Under Uniaxial Compression. *Rock Mech Rock Eng*. 2019;52(7):2067-2085. doi:10.1007/s00603-018-1686-8

9. Ord A, Vardoulakis I, Kajewski R. Shear band formation in Gosford Sandstone. *Int J Rock Mech Min Sci*. 1991;28(5):397-409. doi:10.1016/0148-9062(91)90078-Z

10. Wawersik WR, Fairhurst C. A study of brittle rock fracture in laboratory compression experiments. *Int J Rock Mech Min Sci Geomech Abstr*. 1970;7(5):561-575. doi:10.1016/0148-9062(70)90007-0

11. Tarasov B, Potvin Y. Universal criteria for rock brittleness estimation under triaxial compression. *Int J Rock Mech Min Sci*. 2013;59:57-69. doi:10.1016/j.ijrmms.2012.12.011

12. Drucker DC, Prager W. Soil mechanics and plastic analysis or limit design. *Q Appl Math*. 1952;10(2):157-165. doi:10.1090/qam/48291

13. Zheng Y, Kong L. *Geotechnical Plastic Mechanics*. China Architecture and Building Press; 2010.

14. Zhang S, Wu S, Zhang G, Guo P, Chu C. Three-dimensional evolution of damage in sandstone Brazilian discs by the concurrent use of active and passive ultrasonic techniques. *Acta Geotech*.

2020;15(2):393-408. doi:10.1007/s11440-018-0737-3

15. Zhang S, Wu S, Zhang G. Strength and deformability of a low-porosity sandstone under true triaxial compression conditions. *Int J Rock Mech Min Sci*. 2020;127:104204. doi:10.1016/j.ijrmms.2019.104204

16. Martin CD, Chandler NA. The progressive fracture of Lac du Bonnet granite. *Int J Rock Mech Min Sci*. 1994;31(6):643-659. doi:10.1016/0148-9062(94)90005-1

17. Eberhardt E, Stead D, Stimpson B, Read RS. Identifying crack initiation and propagation thresholds in brittle rock. *Can Geotech J*. 1998;35(2):222-233. doi:10.1139/t97-091

18. Zhao XG, Cai M. A mobilized dilation angle model for rocks. *Int J Rock Mech Min Sci*. 2010;47(3):368-384. doi:10.1016/j.ijrmms.2009.12.007

19. Brace WF, Paulding BW, Scholz C. Dilatancy in the fracture of crystalline rocks. *J Geophys Res.* 1966;71(16):3939-3953. doi:10.1029/jz071i016p03939

20. Bieniawski ZT. Mechanism of brittle fracture of rock: Part II—experimental studies. *Int J Rock Mech Min Sci Geomech Abstr*. 1967;4(4):407-423. doi:https://doi.org/10.1016/0148-9062(67)90031-9

21. Lajtai EZ. Brittle fracture in compression. *Int J Fract*. 1974;10(4):525-536. doi:10.1007/BF00155255

22. Stacey TR. A simple extension strain criterion for fracture of brittle rock. *Int J Rock Mech Min Sci*. 1981;18(6):469-474. doi:10.1016/0148-9062(81)90511-8

23. Diederichs MS, Kaiser PK, Eberhardt E. Damage initiation and propagation in hard rock during tunnelling and the influence of near-face stress rotation. *Int J Rock Mech Min Sci*. 2004;41(5):785-812. doi:10.1016/j.ijrmms.2004.02.003

24. Nicksiar M, Martin CD. Evaluation of methods for determining crack initiation in compression tests on low-porosity rocks. *Rock Mech Rock Eng*. 2012;45(4):607-617. doi:10.1007/s00603-012-0221-6

25. Wu S, Zhang S, Zhang G. Three-dimensional strength estimation of intact rocks using a modified Hoek-Brown criterion based on a new deviatoric function. *Int J Rock Mech Min Sci*. 2018;107:181-190. doi:10.1016/j.ijrmms.2018.04.050

26. Rudnicki JW. Shear and compaction band formation on an elliptic yield cap. *J Geophys Res*. 2004;109(B3):B03402. doi:10.1029/2003JB002633

27. Simo JC, Hughes TJR. *Computational Inelasticity*. Vol 7. Springer Science & Business Media; 2006.

28. Holcomb DJ, Rudnicki JW. Inelastic constitutive properties and shear localization in Tennessee marble. *Int J Numer Anal Methods Geomech*. 2001;25(2):109-129. doi:10.1002/nag.121

29. Issen KA. The influence of constitutive models on localization conditions for porous rock. *Eng Fract Mech*. 2002;69(17):1891-1906. doi:10.1016/S0013-7944(02)00067-X

30. Issen KA, Rudnicki JW. Conditions for compaction bands in porous rock. *J Geophys Res Solid Earth*. 2000;105(B9):21529-21536. doi:10.1029/2000jb900185

31. Perrin G, Leblond JB. Rudnicki and rice's analysis of strain localization revisited. *J Appl Mech Trans ASME*. 1993;60(4):842-846. doi:10.1115/1.2900992

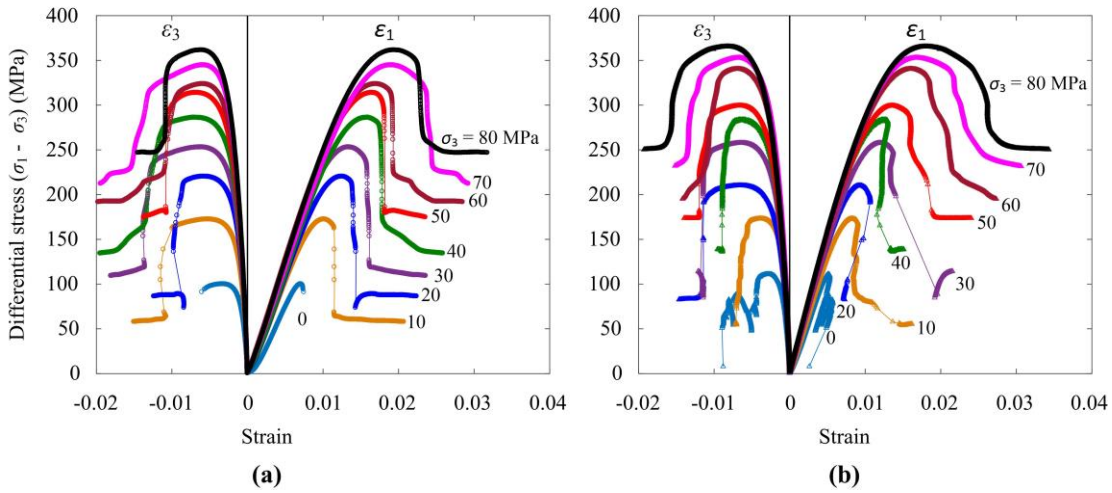

Figure 1 Complete stress-strain curves of **(a)** ASC and **(b)** CSC tests. In both series, the confining pressure σ_3 ranges between 0 and 80 MPa.

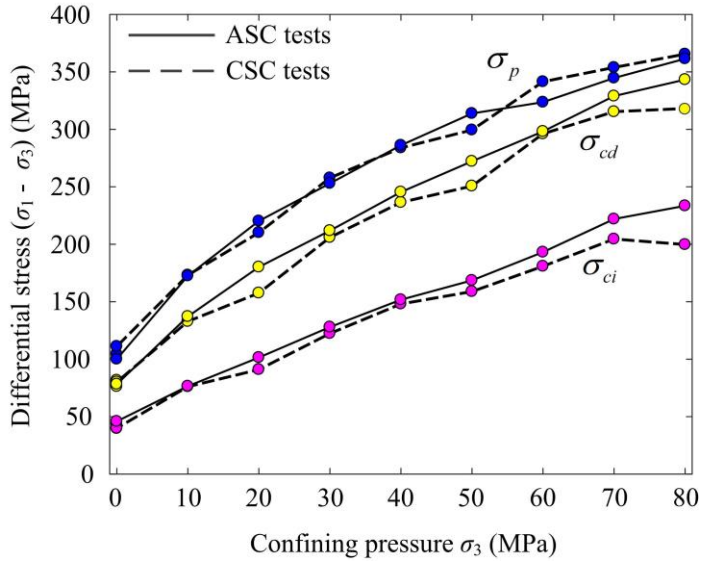

Figure 2 Effect of confining pressure σ_3 on different stress thresholds: crack initiation stress σ_{ci}, crack damage stress σ_{cd}, and peak stress σ_p.

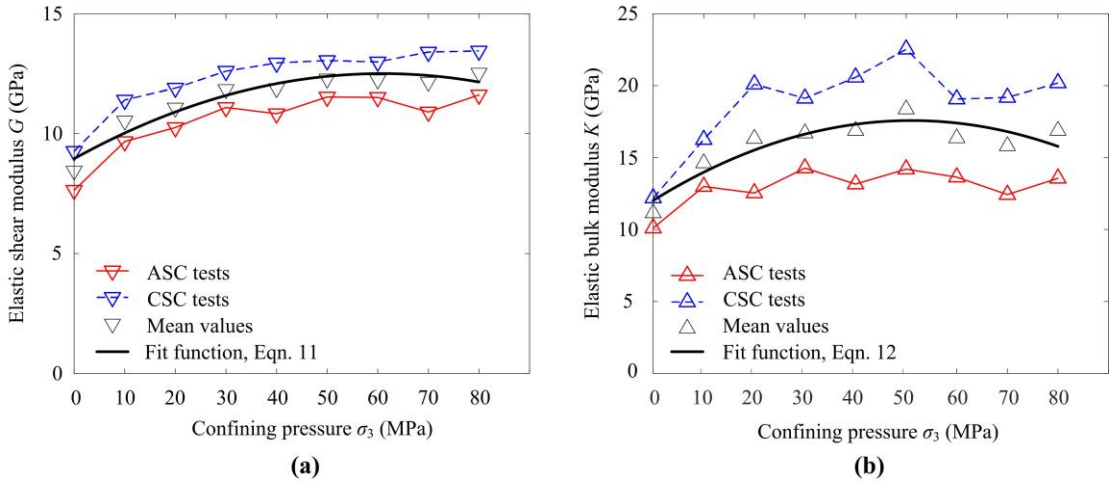

Figure 3 Effect of confining pressure σ_3 on **(a)** elastic shear modulus G and **(b)** elastic bulk modulus K. The black curve denotes the best-fit function of the mean values of each modulus.

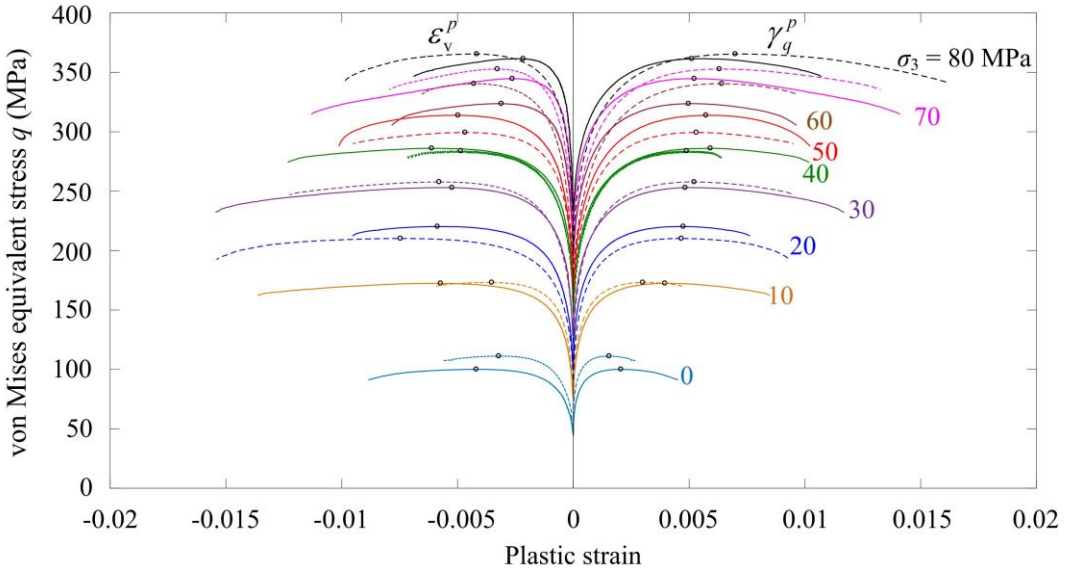

Figure 4 Relationship between von Mises equivalent stress q and two plastic strains, where unstable deformation in the post-peak stage is not shown. Black circles denote peak stresses.

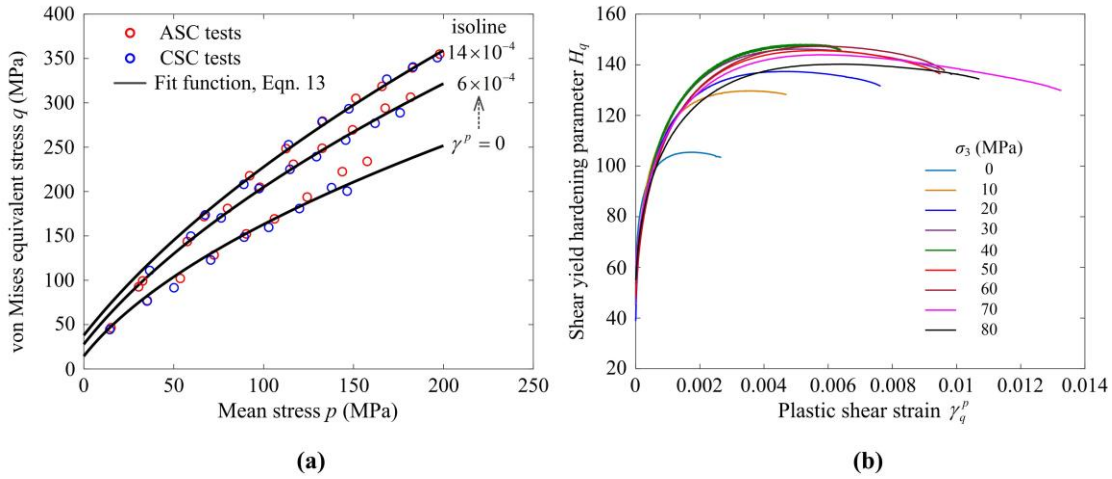

Figure 5 (a) Three representative shear yield surfaces shown as contours of plastic shear strain in *p*-*q* plane. The shear yield surface with zero plastic shear strain is referred to as initial yield surface. **(b)** Relationship between the hardening parameter H_q and plastic shear strain γ_q^p under different confining pressures.

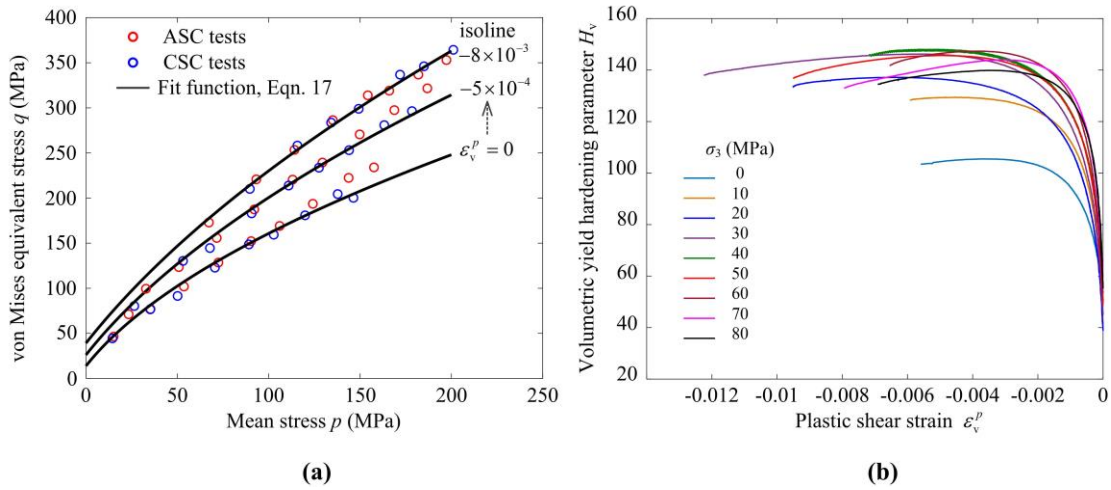

Figure 6 (a) Three representative volumetric yield surfaces shown as contours of plastic volumetric strain in *p*-*q* plane. **(b)** Relationship between hardening parameter H_v and plastic volumetric strain ε_v^p under different confining pressures.

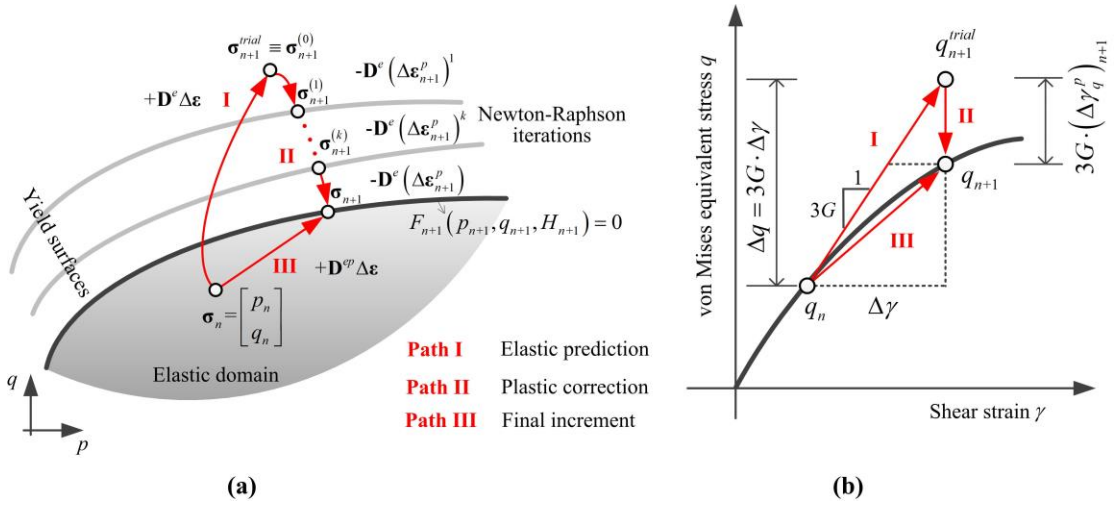

Figure 7 Graphical illustration of the return mapping algorithm: **(a)** general scenario and **(b)** shear yield function.

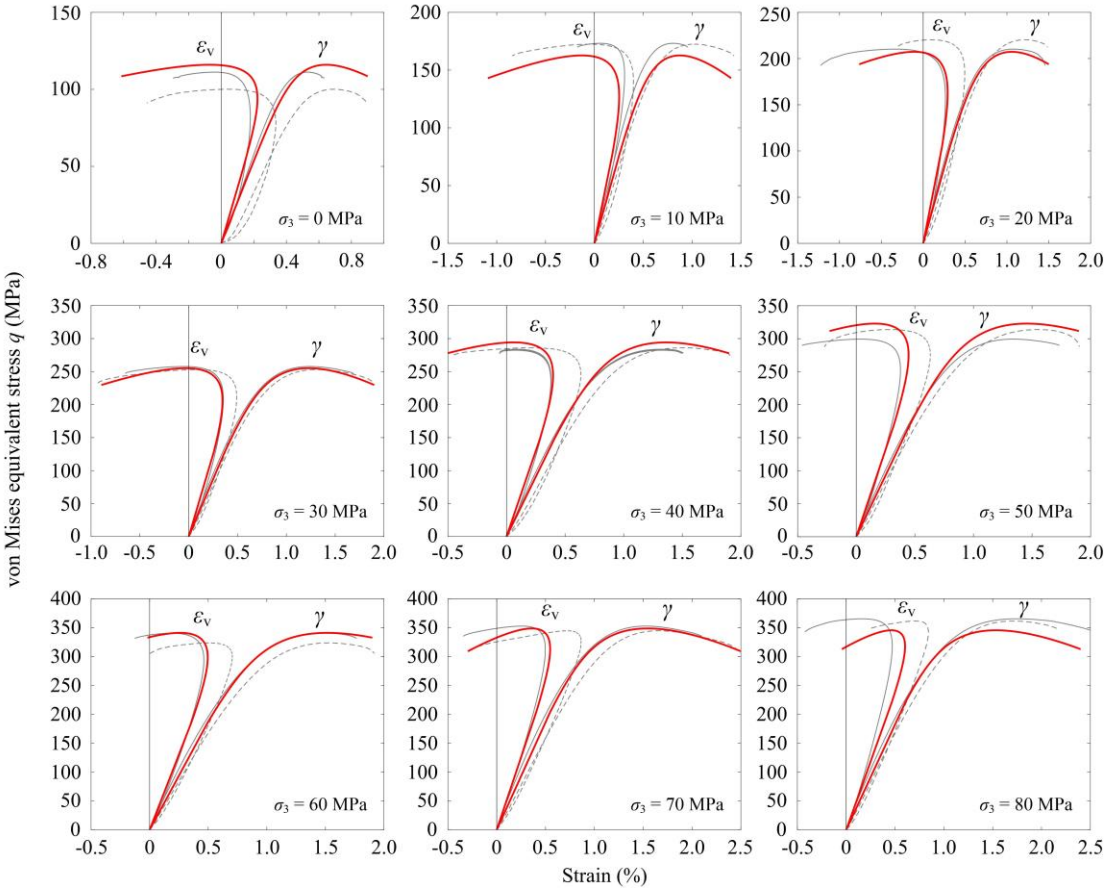

Figure 8 Comparison between the proposed elastoplastic constitutive relationship and experimental results of Zigong sandstone under different confining pressures. Gray solid and dashed lines are from the ASC and CSC tests, respectively, and red solid lines denote numerical simulations.

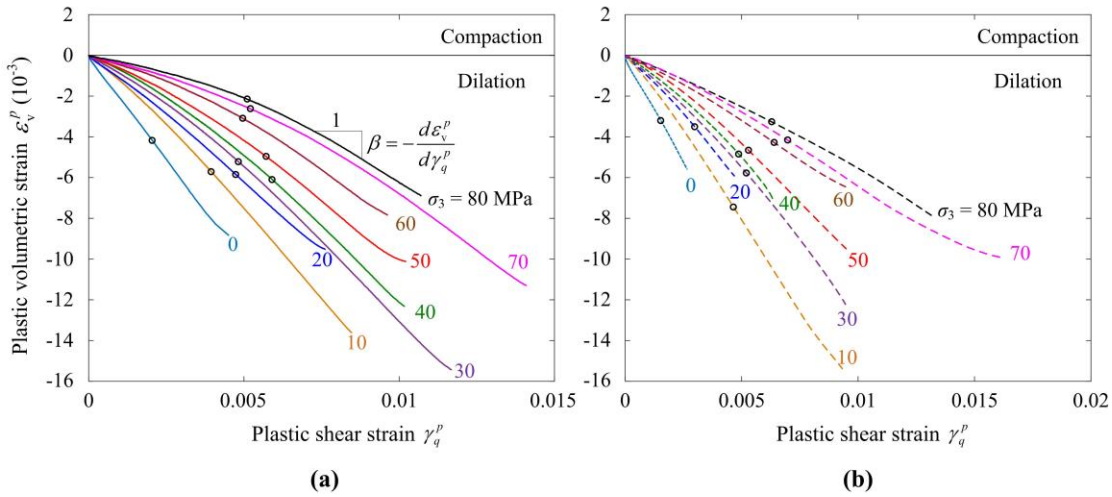

Figure 9 Relationship between the plastic volumetric strain ε_v^p and plastic shear strain γ_q^p under different confining pressures: **(a)** ASC tests and **(b)** CSC tests. On each curve, the black circle denotes the position of peak strength. The definition of the dilatancy factor β is also indicated.

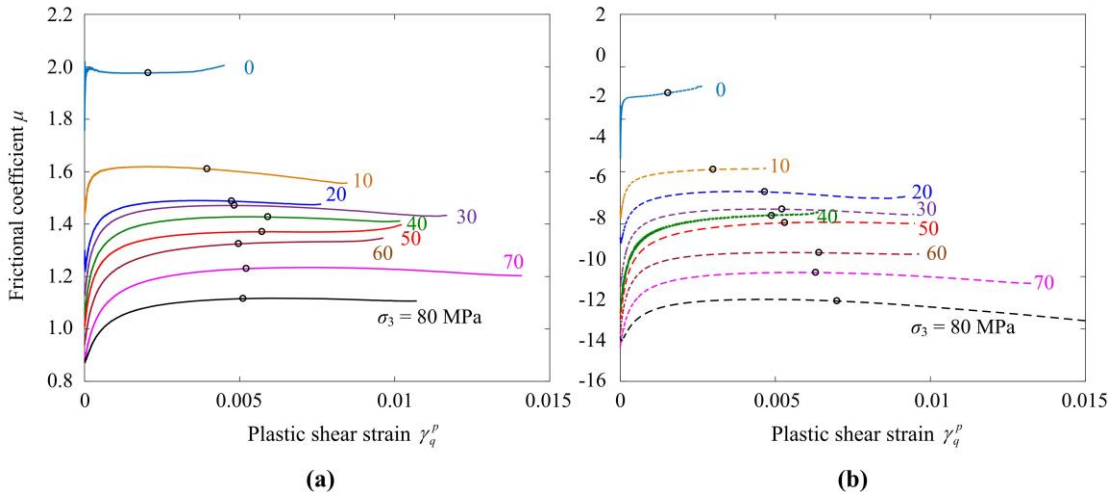

Figure 10 Evolution of frictional coefficient μ with plastic shear strain γ_q^p under different confining pressures: **(a)** ASC tests and **(b)** CSC tests. On each curve, the position of peak strength is indicated by the black circle.

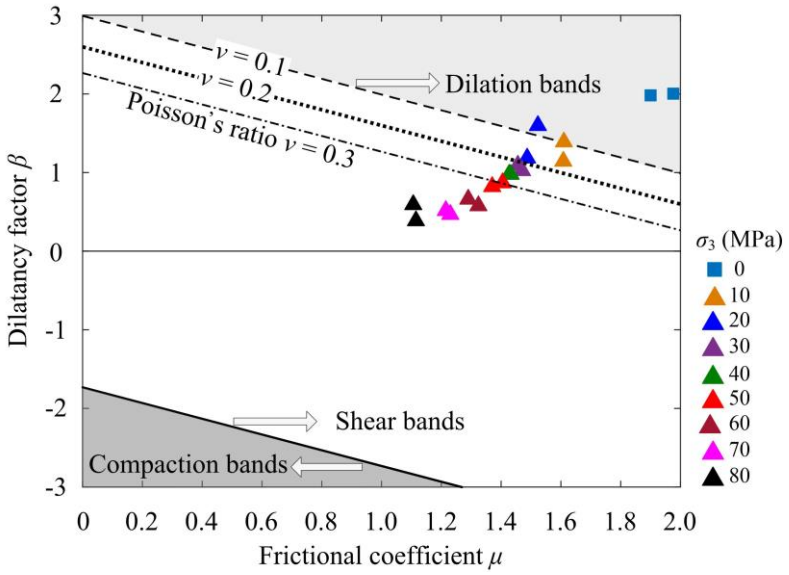

Figure 11 Relationship of constitutive parameters β and μ under different confining pressures. Three reference values (0.1, 0.2, and 0.3) of Poisson's ratio are used to plot the condition for developing dilation bands while the condition for developing compaction bands is indicated by the solid line in the lower left.